

Physical conditions in two high-redshift H₂-bearing GRB-DLAs, 120815A and 121024A.

Gargi Shaw¹★, G. J. Ferland²

¹*Department of Astronomy and Astrophysics, Tata Institute of fundamental research, Homi Bhabha Road, Navy Nagar, Colaba, Mumbai 400005, India*

²*Department of Physics and Astronomy, University of Kentucky, Lexington, KY 40506, USA*

Accepted Received ; in original form

ABSTRACT

The gamma-ray burst (GRB) afterglows provide an unique opportunity to study the interstellar medium (ISM) of star-forming galaxies at high-redshift. The GRB-DLAs (damped Lyman- α absorbers) contain a large neutral hydrogen column density, $N(\text{H I})$, and are observed against the GRB afterglow. A large fraction of GRB-DLAs show presence of molecular hydrogen (H₂) which is an indicator of star-formation. Hence it is important to study those GRB-DLAs which have H₂ lines to decipher and understand their physical conditions. The GRB-DLAs 121024A and 120815A, situated at redshift 2.30 and 2.36 respectively, are two such important H₂-bearing GRB-DLAs. Besides H₂, these two GRB-DLAs also show many metal lines. In this work we have carried out a detail numerical study on the H₂ lines, as well as on those metal lines, in GRB-DLAs 121024A and 120815A self-consistently. We use the spectral synthesis code CLOUDY for this study. This modeling helps us to determine the underlying physical conditions which give rise such lines and hence to understand these two GRB-DLAs in much more detail than any other previous investigation. We find that the hydrogen densities for these two H₂-bearing DLAs are $\geq 60 \text{ cm}^{-3}$. Moreover our study infers that the linear sizes are $\leq 17.7 \text{ pc}$ for these two GRB-DLAs, and the mean gas temperatures averaged over the cloud thickness, are $\leq 140 \text{ K}$. Overall, we find that these two H₂-bearing GRB-DLAs are denser, cooler and smaller compared to those without H₂.

Key words: galaxies: high-redshift, galaxies: ISM, ISM: molecules

1 INTRODUCTION

Molecular hydrogen (H₂) is the first neutral molecule to be formed in the universe, and it is the most abundant and the main constituent of molecular clouds where star formation takes place (Burton 1992; Tielens 2005; Bigiel et al. 2008). Furthermore, H₂ controls most of the chemistry in ISM through its ionic or neutral form. In addition to these, level populations of H₂ in various levels can be used as tracers for physical conditions. For example, in the well-shielded H₂ gas the lower rotational levels of the ground state of H₂ are mostly collisionally dominated, hence they are in LTE, and can be used to infer gas temperature (Abgrall et al. 1992). Whereas, the higher levels are generally populated

by non-thermal processes and can be used to estimate ambient radiation field (Draine & Bertoldi 1996; Shaw et al. 2005) and the cosmic ray ionisation rate of hydrogen (Tineé et al. 1997). As a result, H₂ spectra provide an excellent opportunity to probe star formation and chemical enrichment of galaxies ranging from local to high-redshift (z).

In Milky Way, a large neutral hydrogen column density $N(\text{H I})$ is in general associated with H₂ (Savage et al. 1977; Winkel et al. 2017; Marasco et al. 2017). If the physical conditions of high- z galaxies are similar to that of Milky Way, it is expected that large $N(\text{H I})$ regions at high- z galaxies are also associated with H₂. Therefore, chemical evolutions of these high- z galaxies can also be studied through systems with large $N(\text{H I})$. The damped Lyman- α systems (DLAs) are such systems with a large $N(\text{H I})$ (Wolfe et al. 2005) and which are also the main reservoir of neutral gas at high- z .

DLAs can be probed using absorption spectroscopy against distant bright sources, such as quasi-stellar objects (QSOs) or gamma-ray bursts (GRBs). DLAs observed against the QSOs are called QSO-DLAs, whereas, DLAs de-

★ E-mail: gargishaw@gmail.com

tected against the GRB afterglow are called GRB-DLAs. The long GRBs, with a duration greater than two seconds, are believed to be originated from the core-collapsed supernova. Since massive stars are short lived and are located in star-forming regions of galaxies, it is apparent that GRBs are also associated with star-forming regions of a galaxy (Woosley 1993). An excellent review of GRB-DLAs in the Swift era is provided by Schady (2017).

To date, many QSO-DLAs and GRB-DLAs have been observed by several groups (Prochaska et al. 2001; Srianand et al. 2005b; Ledoux et al. 2003; Daniel et al. 2008; Toy et al. 2016; Ledoux et al. 2009; Heintz et al. 2019; Bolmer et al. 2019) etc. The GRB-DLAs are smaller in number than QSO-DLAs as GRBs are transitory in nature. However, the GRB-DLAs show larger $N(\text{H I})$ and higher metallicity than those of QSO-DLAs (Prochaska et al. 2007). Here, metallicity relative to solar is expressed as $[X/H] = \log[N(X)/N(H)] - \log[N(X)/N(H)]_{\odot}$ (with $X = \text{Zn}$, or Si , or S). It was also noticed by Cucchiara et al. (2015) that at high- z the average metallicity of QSO-DLAs decline at a faster rate than GRB-DLAs. In general, QSO-DLAs probe diffuse gas and hence they are not suitable to study star formation. On the contrary, since GRBs are located inside the galaxies, GRB-DLAs probe inner regions of galaxies (Fynbo et al. 2008), and consequently, GRB-DLAs are much suitable for studying star-forming regions. However, recent studies of extremely saturated DLAs (ESDLA) (Noterdaeme et al. 2014, 2015a; Balashev et al. 2017; Ranjan et al. 2018; Bolmer et al. 2019; Ranjan et al. 2020) indicate that ESDLAs and GRB-DLAs likely represent the same population of the galaxies, probed by small impact parameters, and hence can probe star-forming regions. Furthermore, recently, a huge data is also available on GRB-DLA host galaxies up to a very high redshift ($z \approx 6$) (Hartoog et al. 2015; Bolmer et al. 2019).

Initially, Tumlinson et al. (2007) studied five GRB-DLAs but did not find H_2 in spite of large $N(\text{H I})$. They concluded that this lack of H_2 may be due to a combination of low metallicity and an FUV radiation field of 10-100 times the Galactic mean field. Later, Ledoux et al. (2009) observed seven $z > 1.8$ GRB afterglows with VLT/UVES but they also did not find H_2 in their sample. They explained the lack of detected H_2 through the low metallicities, low depletion factors, and moderate particle densities of these systems. Though Tumlinson et al. (2007) and Ledoux et al. (2009) differed regarding the FUV radiation field, they both agreed on the low metallicity of these systems. Ledoux et al. (2009) estimated a particle density of $5\text{--}15 \text{ cm}^{-3}$, a linear cloud size of 520_{-190}^{+240} pc, and the kinetic temperature > 1000 K for these seven $z > 1.8$ GRB afterglows of their sample which did not show H_2 . Later Toy et al. (2016) observed a sample of 45 GRB-DLAs in the redshift range of 2 to 6 and they found that DLA counterpart star formation rates (SFRs) are not correlated with either redshift or H I column density.

However, some other GRB-DLAs, which harbour H_2 , were found, namely, GRB-DLA 80607, GRB-DLA 121024A, GRB-DLA 120815A and GRB-DLA 120327A at redshifts 3.03, 2.30, 2.36 and 2.8 (Sheffer et al. 2009; Friis et al. 2015; Krühler et al. 2013; D’Elia et al. 2014). Recently Bolmer et al. (2019) have observed 22 GRB-DLAs with VLT/X-shooter for $z > 2$. In their sample, they found H_2 absorption lines in 6 out of these 22 GRB-DLAs, which also include

GRB-DLA 121024A, GRB-DLA 120815A and GRB-DLA 120327A. They concluded that there is no lack of detected H_2 for GRB-DLAs and the detection rate is much higher in GRB-DLAs than the QSO-DLAs. It has been noted that for GRB-DLAs with $\log N(\text{H I}) > 21.7$, the detection of molecular hydrogen increases (Bolmer et al. 2019). The same increase in the detection rate at high H I is also seen in QSO-DLAs (Noterdaeme et al. 2015a; Balashev & Noterdaeme 2018). Earlier, such conversion of H I to H_2 was analytically studied (Sternberg 1988; Sternberg et al. 2014), and observationally constrained for both low and high redshifts (Savage et al. 1977; Welty et al. 2016; Noterdaeme et al. 2015a; Balashev & Noterdaeme 2018). It is thus natural to ask whether the physical conditions of H_2 -bearing DLAs are quite different than those without H_2 , and if so, how to probe and then understand that. One of the plausible answers for detectable H_2 could be the presence of dust grains, higher metallicity, and higher density. Dust grains are very important as their surfaces act as a catalyst for efficient H_2 formation. As an example, it has been suggested by many observers (Srianand et al. 2005a,b) that the H_2 -bearing QSO-DLAs might have higher density and higher dust content compared to the non H_2 -bearing QSO-DLAs.

A detail numerical spectroscopic modeling of GRB-DLAs considering all the possible microphysics of H_2 is thus quite crucial to determine the underlying physical conditions which give rise such lines, and hence to understand these systems which harbour H_2 . Previously, Whalen et al. (2008) had carried out a numerical simulation to understand the absence of H_2 in GRB-DLAs. However, so far, no one has performed any detail microscopic modelling of such systems which harbour H_2 . Previously, we successfully carried out several detail modelings of QSO-DLAs (Srianand et al. 2005a,b; Shaw et al. 2016; Rawlins et al. 2018) with detected H_2 lines. Following that in this work, we employ the spectral synthesis code CLOUDY (Ferland et al. 2017) for a microscopic detail modelling with an aim to understand the physical conditions of H_2 -bearing GRB-DLAs.

Our calculation incorporates detail microphysics both at atomic and molecular levels including collisional physics and line shape theory. In this work we choose following two systems: GRB-DLAs 121024A and 120815A, and study them self-consistently. We select these two GRB-DLAs as they have higher molecular fraction with $\log(f) \approx -1.14 \pm 0.15$ and -1.4 , respectively, and so will serve our purpose best to distinguish H_2 -bearing from non- H_2 -bearing GRB-DLAs. In addition to H_2 , these two DLAs show numerous metal lines together with the rest frame UV absorption lines of H_2 . Along with H_2 lines, above mentioned extra lines are also modeled self-consistently in our calculation.

This article is organized as below: in section 2 we give details of our calculation using CLOUDY. Detail of microphysics incorporated in our calculation is also provided. In section 3 we present the findings from this study, first providing results for GRB-DLA 120815A and then for GRB-DLA 121024A. Summary and conclusions are presented in section 4.

2 CALCULATIONS

CLOUDY is a self-consistent stationary micro-physics code based on *ab initio* calculation of thermal, ionisation, and chemical balance of non-equilibrium gas and dust exposed to a source of radiation. It predicts column densities of various atomic and molecular species and resultant spectra covering the whole range of EM radiation and vice versa using a minimum number of input parameters. It has a state-of-the-art detailed H₂ network (Shaw et al. 2005) embedded which is very helpful for modelling environments with H₂. The H₂ network includes 301 rovibrational levels within the ground electronic state and also the rovibrational levels within the lowest six electronic excited states.

Here, we briefly discuss the main formation and destruction processes of H₂ that are implemented inside CLOUDY and affect the H₂ level populations. Since the formation process of H₂ is exothermic and the resulting energy for such process is close to its dissociation energy, H₂ formation does not simply take place in gas phase by interaction of two H atoms. It requires a mechanism to take away some of the formation energy to form a stable H₂ molecule. In a dusty environment, dust plays the role to share that formation energy. As a result, H₂ is mainly formed on dust grain surfaces where dusts can act as a catalyst and take away some of the formation energy. In a dust-free environment, H₂ can still form through an exchange reaction of H with H⁻ (Launay et al. 1991) and H₂⁺ (Kristic 2002) but the reaction rates are smaller. The main destruction and excitation mechanism for H₂ is the photoexcitation. In this process, H₂ absorbs Lyman and Werner band photons and gets excited to higher electronic levels. Of these excited populations, 10-15% comes down to the continuum of ground electronic state and get dissociated. The rest populates higher vibrational levels of the ground electronic state (Abgrall et al. 1992). Besides this, the formation process is exothermic, hence the dust grains also play a crucial role in the distribution of level population of newly formed H₂ on dust grain surfaces (Black & van Dishoeck 1987; Le Bourlot et al. 1995; Draine & Bertoldi 1996; Takahashi & Uehara 2001). Note that deep into the cloud, excitation by secondary electrons produced by cosmic ray is also an important H₂ level excitation mechanism (Tineé et al. 1997). All these above mentioned processes are incorporated inside CLOUDY and details are given in Shaw et al. (2005) and Gay et al. (2012). It is well known that depending on the nuclear spin orientations, H₂ can be in one of the two quantum states, namely, ortho or para. In an ortho state, the nuclear spins are aligned parallel, whereas in a para state, they are anti-parallel. Note that radiative transitions are not possible between ortho and para states of the ground electronic level and only reactive collisions with H⁰, H⁺, and H⁺³ (Sun & Dalgarno 1994; Gerlich 1990; Le Bourlot 1991) are capable to make transitions between these quantum states. In our H₂ network, CLOUDY includes both reactive and non-reactive collisions. For details, see (Shaw et al. 2005).

2.1 Modelling

For all the models that we incorporated in this work, we assume a plane-parallel constant pressure gas exposed to radiation. We vary a few free parameters, as will be discussed

below, to match the predicted column densities with the observed column densities of various atoms, ions and state specific H₂. The chosen radiation field has three components: a meta-galactic radiation at appropriate redshift (Haardt & Madau 2012), a synchrotron radiation (power-law continuum) arising from GRB afterglow and a blackbody radiation from *in situ* star formation. Our GRB-DLA models are similar to our previous QSO-DLA models (Srianand et al. 2005a; Shaw et al. 2016; Rawlins et al. 2018) except that here we have an additional synchrotron radiation arising from GRB afterglows. While the gas is exposed to UV radiation from everywhere it is exposed to GRB afterglow only from one side.

In the current CLOUDY set up, it is not possible to consider both two-sided and one-sided radiation fields simultaneously in a same model. Hence we consider following two cases separately: Case 1, where we assume that the gas cloud is irradiated from both sides; and Case 2: where we assume that the gas cloud is irradiated from one side. We present our results for both the cases. The models presented here show that this does not effect the conclusions. However, it need to be noted that the geometry of the cloud is unknown and might be unknowable. The time history of the cloud is not known and we are also using a stationary code. These can also affect the results.

2.2 Input parameters

In this work, we use the dimensionless ratio of hydrogen-ionising photon $Q(H)$ (s⁻¹) to total-hydrogen densities $n(H)$ (cm⁻³) in order to quantify the radiation field, and denote it by ionisation parameter, χ , as,

$$\chi = \frac{Q(H)}{4\pi r_0^2 c n(H)}. \quad (1)$$

Here r_0 and c are the separation (cm) between the center of the source of ionizing radiation and the illuminated face of the cloud, and the speed of light, respectively.

We consider both graphite and silicate grains in the calculations with MRN (Mathis et al. 1977) size distribution over ten size bins in the range 0.005 to 0.25 micron (ISM grains). For MRN grains, the grain size distribution varies as $a^{-3.5}$, where a is the radius of the grain. Beside that, dusts provide heating through photoelectric heating, as well as it shields interior regions of molecular cloud from far-ultraviolet (FUV) radiation. The detail grain physics included in CLOUDY was described in van Hoof et al. (2004). It has been observed that dust is correlated with metallicity, and in general, metallicity is anti-correlated with redshift. It is believed that Fe is strongly depleted on dust grains whereas Zn is not depleted. Hence, one can estimate the metallicity and dust-to-gas ratio with the help of Zn/H and Fe/Zn ratios (Prochaska & Wolfe 2002). In our models, both metallicity and dust-to-gas ratio are derived using column densities of Zn, Fe and equation no. 1 from Prochaska & Wolfe (2002).

As mentioned earlier, cosmic ray affects the level populations of H₂ via secondary electrons which are produced by cosmic ray ionisation (Tineé et al. 1997). However, the cosmic ray ionisation rate is not the same along all line-of-sights (Indriolo et al. 2007; Shaw et al. 2008a). Since not much is

known on the cosmic ray ionisation rate at high-redshift, we consider this rate as a free parameter in our models.

We also treat the total hydrogen density, which includes all forms of hydrogen bearing chemical species, as a free parameter in our models. To be noted that CLOUDY requires at least one suitable stopping criterion for each model and it will stop calculations at some depth of the cloud depending on the stopping criterion. These stopping criteria vary depending on particular observed quantities that one match with. For all our case 2 models, we consider the observed total H_2 column densities as the stopping criterion, i.e., CLOUDY will continue its calculation till a depth of the cloud where the predicted total H_2 column density matches well with the corresponding observed value. Whereas, for case 1, we stop the model at a depth in the cloud where the total H_2 column density equals half of the observed H_2 column density. Finally we multiply our predictions by 2 to mimic the situation where the cloud is irradiated from both sides.

A built-in optimization program, based on pymir algorithm (van Hoof 1997), which calculates a non-standard goodness-of-fit estimator χ^2 and minimises it by varying input parameters, is employed to identify the best model. Sometimes, to reach to the final model of a calculation, a few parameters are fine tuned so that the observed data can be matched maximally. This optimisation program is user friendly and has been utilised extensively in many previous works (Ferland et al. 2013; Srianand & Petitjean 2000; Shaw et al. 2006; Rawlins et al. 2018; Shaw & Bhattacharyya 2019).

In this work, using various parameters as discussed above, our main focus is to model the observed state-specific H_2 column densities self-consistently together with other observed column densities of ionic, atomic and molecular species to understand the underlying physical conditions which play pivotal roles to generate them. Below we discuss our findings.

3 RESULTS

In this section, results and main findings are elaborated. First GRB-DLA 120815A is discussed in detail, followed by GRB-DLA 121024A.

3.1 GRB-DLA 120815A

For the GRB-DLA 120815A, H_2 lines were first detected at $z = 2.36$ by Krühler et al. (2013). They observed the line-of-sight using X-shooter at VLT. H_2 absorption lines were observed in the rest frame Lyman and Werner bands (11.2–13.6 eV) which have been shifted to optical band due to redshift and hence could be easily observed by X-shooter which is an optical telescope. They reported H_2 column densities for the first four rotational levels of ground state. The neutral carbon and H_2 gets photo-dissociated by photons of the same energies, and hence the neutral carbon generally co-exists with H_2 (Noterdaeme et al. 2007, 2018; Jorgenson et al. 2009). As expected, the neutral carbon was also observed in this GRB-DLA. Beside H_2 , they also detected various metal lines, such as Zn, S, Si, Mn, Fe, Ni in their first ionisation states. The observed metallicity ($[Zn/H]$) and

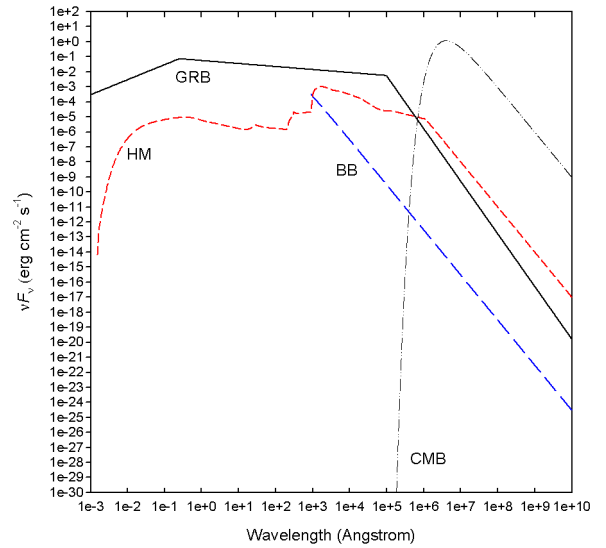


Figure 1. The SED of the individual components of incident radiation field for GRB-DLA 120815A. The dash-dotted (black) and medium-dashed (red) lines represent CMB and Haardt-Madau metagalactic radiation field at $z=2.36$, respectively. The long-dashed (blue) line represents extinguished (no H-ionising radiation) stellar radiation generated using black body radiation at 10^5 K. The solid black line represents the powerlaw continuum from the GRB. The powerlaw continuum behaves as $\nu^{5/2}$ at lower energy to account for self-absorbed synchrotron (Rybicki & Lightman 1979), ν^{-2} at higher energies and -0.8 between 10 micron and 50 KeV.

dust depletion ($[Zn/Fe]$) were found to be -1.15 ± 0.15 and 1.01 ± 0.10 , respectively. Using these the dust-to-gas ratio is calculated to be ≈ 0.06 of the local ISM value, and is used in our models. They also found the broadening parameter of the H_2 lines to be 8.7 ± 0.6 km s $^{-1}$. In our model, we fix the microturbulence/broadening parameter to the observed value 8 km s $^{-1}$.

As mentioned previously, in our model we consider that radiation consists of a meta-galactic background at $z=2.36$, a blackbody radiation from an *insitu* star formation and a power law continuum due to afterglow. Krühler et al. (2013) found a power law slope of -0.78 as the best-fit value. Furthermore, recently, Li et al. (2018) have published a large catalogue of multi-wavelength GRB afterglows with spectral indices of 70 GRBs, and they have mentioned -0.78 ± 0.01 as the spectral index for GRBs 120815A. Based on these facts, we choose -0.8 as the spectral index for GRB. As an example, in Fig.1 we plot all the components of the SED for GRB-DLA 120815A (case 1). The corresponding UV field is equivalent to 7 Habing. Case 2 also has the similar features with corresponding UV field 6.6 habing. In Table 1 we list the model parameters corresponding to our best model and the second and third columns represent Case 1 and Case 2, respectively. In case 1, our model predicts a hydrogen density of 440 cm $^{-3}$. Whereas, for case 2 the predicted hydrogen density is lower, 230 cm $^{-3}$. For other elements, whose lines were observed, we vary their abundances in our model to match their observed values while keeping the abundances of other elements at 0.07 of the ISM value. Final values of metal abundances of Zn, S, Si, Fe, Ni, Cr and Mn, that we obtain

Table 1. Physical parameters for GRB-DLA 120815A using CLOUDY.

Physical parameters	best values	best values
	Case 1	Case 2
Power law: $\log(\chi)$	-4.2	-4.0
Black body: Temperature (log K), $\log(\chi)$	5.0, -1.8	5.3, -2.6
Density $n(\text{H})$ (cm^{-3})	440	230
Cosmic ray ionisation rate (10^{-16} s^{-1})	1.9	1.9
[Fe/H]	-2.24	-2.27
[Mg/H]	-1.93	-1.89
[C/H]	-2.39	-2.39
[Zn/H]	-1.28	-1.27
[Ni/H]	-2.17	-2.19
[Mn/H]	-2.27	-2.27
[Cr/H]	-2.07	-2.04
[S/H]	-1.48	-1.20
[N/H]	-1.18	-1.18
[O/H]	-1.33	-1.33

from our best fit model, match well with the observed data (within the observed error bars) by Krühler et al. (2013). In addition to these, we also predict the abundances of C, O, N and Mg. Krühler et al. (2013) have measured the $A_V = 0.15 \pm 0.02$ along this sight line. However, we predict $A_V = 0.32$ and 0.31 for case 1 and case 2, respectively. These are higher than the observed value. We also find that the cosmic ray ionisation rate of hydrogen along this line-of-sight is approximately $2 \times 10^{-16} \text{ s}^{-1}$, similar to the average galactic value reported by Indriolo et al. (2007). In Table 2 we compare the observed data and our model predicted column densities in two different columns. To be noted that in addition to the observed species, observable amount of OH and OH⁺ with column density $> 10^{13} \text{ cm}^{-2}$ are also predicted by our models. One can see that our model predicts the rotationally resolved H₂ column densities within the observed range, except for rotation level $J = 2$.

Different parameters affect the predicted column densities to different amounts. To see the variation in predicted column densities due to change in parameters, we vary the important parameters by 0.3 dex around their values used in the best model (Case 1). In Table 3 we present this change in predicted column densities (in dex). We would like to emphasize here that the stopping criterion, i.e., total H₂ column density, remains the same for each set of parameters. Our calculation shows that among all parameters the effect of dust grains is the maximum. Similar trend is observed for case 2.

As we know that numerical models can be utilized to predict various physical conditions across the cloud which are not possible by today's observations. In our model we also calculate the abundances of $\text{H}^0/\text{H}_{total}$, $\text{H}^+/\text{H}_{total}$, $2\text{H}_2/\text{H}_{total}$ and the variation of gas temperature across the cloud, Figs. 2 and 3 show those for Case 1 and case 2, respectively. Fig.1 shows half of the cloud, and the other half is its reflection. Our best models predict the size of the GRB-DLA 120815A to be 9.8 and 17.7 parsec for case 1 and case 2, respectively. Interestingly, this linear size is much smaller than that reported by (Ledoux et al. 2009) for GRB-LAs with no H₂. The gas temperature is one of the important physical conditions for any astrophysical environment. It is well known that in the warm phase of the ISM, $T > 1000 \text{ K}$

Table 2. Comparison of observed and predicted column densities (in log scale) for GRB-DLA 120815A using CLOUDY.

Species	observed (cm^{-2})	predicted	predicted
		(cm^{-2}) Case 1	(cm^{-2}) Case 2
H I	21.95 ± 0.10	22.10	22.08
H ₂	20.54 ± 0.13	20.54	20.54
Mg I	13.54 ± 0.05	13.48	13.49
Ni II	14.19 ± 0.05	14.17	14.17
Zn II	13.47 ± 0.06	13.44	13.44
C I	13.41 ± 0.11	13.41	13.43
Fe II	15.29 ± 0.05	15.34	15.26
Mn II	13.26 ± 0.05	13.22	13.16
Cr II	13.75 ± 0.06	13.73	13.74
S II	$\leq 16.22 \pm 0.25$	15.90	16.17
Si II	$\geq 16.34 \pm 0.16$	16.00	15.85
CO	< 15.0	11.60	11.50
OH	–	13.85	13.85
OH ⁺	–	13.16	13.36
HCl	–	12.67	12.46
H ₂ O	–	12.54	12.42
H ₂ O ⁺	–	12.41	12.46
H ₃ ⁺	–	12.42	12.51
H ₂ (0)	19.84 ± 0.33	20.02	19.98
H ₂ (1)	20.43 ± 0.12	20.37	20.38
H ₂ (2)	16.76 ± 0.50	18.89	19.01
H ₂ (3)	≤ 19.01	17.91	17.99
H ₂ (total)	20.54 ± 0.13	20.54	20.54

and $n < 10 \text{ cm}^{-3}$. Whereas, in the dense cold phase $T \sim 100 \text{ K}$ and $n > 100 \text{ cm}^{-3}$. For Case 1, the predicted gas temperature remains almost constant near 120 K. On the contrary, for case 2 the gas temperature ranges from 157 K to 129 K with an average of 142 K over the linear extension of the cloud. In a collisionally dominated environment, $J = 1$ and 0 levels of H₂ are generally thermalised and can be used to determine the surrounding gas temperature. This excitation temperature, T_{10} , is calculated using the following equation,

$$T_{10} = -170.5 \left[\ln \frac{N(J=1)}{9N(J=0)} \right]^{-1} \text{ K}. \quad (2)$$

Here $N(J = 1)$ and $N(J = 0)$ are column densities in the $J = 1$ and 0 levels of H₂, respectively, separated by the energy gap equivalent to 170.5 K. For this source, the observed T_{10} ranges from 90 to 480 K, matching with our prediction of the average temperature mentioned earlier. Both the temperatures are cooler than the GRB-DLAs without H₂. This suggests that the H₂-bearing GRB-DLAs trace the cold neutral phase of the ISM. It is to be noted that, the kinetic temperature is directly measured for H₂-bearing DLAs. Whereas, it is not well constrained for non-H₂-bearing DLAs. Though, so far, there is no observational data on 21 cm absorption for this source, we calculate the excitation temperature of the hyperfine levels involved in 21cm transition (T_{21cm}) using,

$$T_{21cm} = -0.068 \left[\ln \frac{N_2}{3N_1} \right]^{-1} \text{ K}. \quad (3)$$

Here, N_2 and N_1 are column densities of the hyperfine levels $^1S_{1/2}$ and $^0S_{1/2}$ (Urbaniak & Wolfe 1981; Deguchi & Watson 1985; Field 1959), respectively, separated by the energy gap equivalent to 0.068 K. Previously Shaw et al. (2017)

Table 3. Variation in column densities of GRB-DLA 120815A (in dex) for variation of different input parameters (Case 1).

Species	$\Delta n(\text{H})$	Δgrain	$\Delta \log(\chi)$
	0.3 dex	0.3 dex	power law -0.3 dex
H I	0.02	-0.30	-0.20
Mg I	-0.01	-0.35	0.04
Ni II	-0.07	-0.38	-0.22
Zn II	0.01	-0.28	-0.20
C I	-0.02	-0.32	-0.04
Fe II	0.01	-0.28	-0.22
Mn II	0	-0.27	-0.22
Cr II	0.01	-0.28	-0.21
S II	0.02	-0.28	-0.22
CO	0.10	0.21	0.27
OH	0.08	0.22	0.05
OH ⁺	0.01	-0.10	0.25
HCl	0.03	-0.06	0.03
H ₂ O	0.14	0.39	0.21
H ₂ O ⁺	0.85	0.14	-0.13
H ₃ ⁺	0	0.18	0
H ₂ (0)	-0.03	-0.05	0.07
H ₂ (1)	0	0.01	-0.03
H ₂ (2)	0.10	0.16	-0.20
H ₂ (3)	0.24	0.13	-0.31

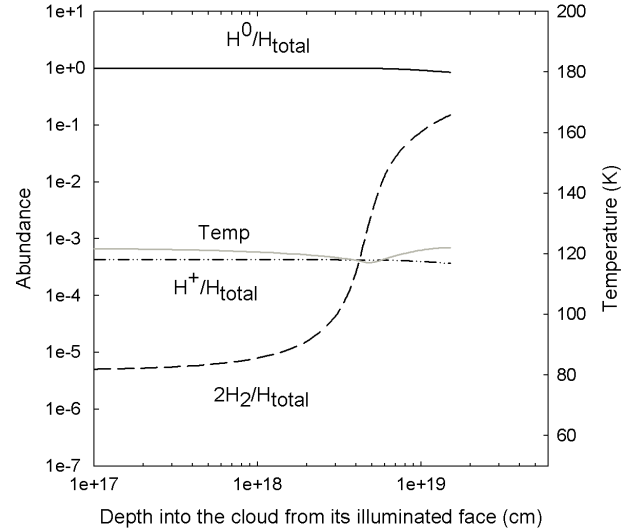
described all the possible excitation and de-excitation processes of the hyperfine levels related to 21 cm transition, as incorporated by CLOUDY. It includes collisional excitations and de-excitations by H^0 , e^- and H^+ , together with the non-thermal radiative processes including direct pumping by the 21 cm radio continuum, pumping by the continuum near $\text{Ly}\alpha$, and by the $\text{Ly}\alpha$ line itself. Here we find $T_{21\text{cm}}$ to be 508 K and 1006 K for case 1 and case 2, respectively. This is higher than the kinetic temperature. Similar trend had also been observed for the QSO-DLA at redshift 1.78 along Q1333+ (Chengalur & Kanekar 2000; Cui et al. 2005).

In our models the gas temperature is determined by heating and cooling balance where various processes contribute to the total heating and cooling. We find that the grain photoelectric heating is the dominant heating processes for this source. In the grain photoelectric heating, a dust grain absorbs a FUV photon and emits energetic electrons which heats up its surrounding region by collisions. We find that the grain photoelectric heating diminishes deep inside the cloud as FUV decreases inside the cloud. On the other hand, fractional heating by cosmic ray ionisation increases as one moves inside the cloud. The dominant coolants are found to be O I and C II lines.

We would like to emphasize here that for both cases we find the GRB-DLA 120815A is denser, smaller, and cooler than that reported by Ledoux et al. (2009) for GRB-DLAs with no H_2 . Next we discuss GRB-DLA 121024A.

3.2 GRB-DLA 121024A

In this section, we present our findings for another H_2 -bearing GRB-DLA: GRB-DLA 121024A. The first trigger of GRB-DLA 121024A was reported in 2012. Later, Friis et al. (2015) observed numerous absorption and emission lines spanned over five components. However, H_2 was detected in

**Figure 2.** Temperature and $\text{H}^0/\text{H}_{\text{total}}$, $\text{H}^+/\text{H}_{\text{total}}$, $2\text{H}_2/\text{H}_{\text{total}}$ are plotted as a function of distance into GRB-DLA 120815A (Case 1). The temperature axis is shown in the right. This plot shows half of the cloud. The other half is just the reflection of this portion.

only three out of five components (c+d+e) in rest frame Lyman and Werner band. They derived H_2 in its lowest four rotational states of the ground vibrational level ($J = 0, 1, 2, 3$). However, CO (< 14.4) was not detected even though H_2 was detected. In addition to these, many metal lines of the metals Fe, Ni, Cr, Mn, Ca, Zn were present in their first ionised state. The reported metallicity ($[\text{Zn}/\text{H}]$) and dust depletion ($[\text{Zn}/\text{Fe}]$) are observed to be -0.6 ± 0.2 and 0.85 ± 0.04 , respectively. Using these the dust-to-gas ratio is calculated to be ≈ 0.2 of the local ISM value.

Though the component wise column densities were reported for metal lines, the component wise H_2 and H I column densities were not provided. Hence, we add up the three H_2 -bearing components and consider them as a single component, and try to decipher the physical conditions of this stratified component. They have mentioned that the total H I column density for this stratified component is $10^{21.6} \text{ cm}^{-2}$. In this calculation we use the metallicity and dust-to-gas ratio to the observed value. Friis et al. (2015) used -0.9 ± 0.02 as the spectral index for the GRB afterglow. In addition to this, Li et al. (2018) also observed -0.86 ± 0.01 as the spectral index for GRB 121024A. Keeping the observed value in mind, we fix the slope for the power law continuum to -0.9 . Similar to our study of previous DLA, here also in our calculations we consider Case 1 and 2. The individual components of the SED have similar features as shown in Fig. 1. The equivalent UV fields are 15 and 28 Habing for cases 1 and 2, respectively. Below we presents our results for these two cases.

We list our best model parameters for these cases in the second and third columns of Table 4. The abundances of the elements, whose lines have been observed, are varied to match their observed values. The predicted hydrogen density is 100 cm^{-3} and 60 cm^{-3} for case 1 and case 2, respectively. Beside hydrogen density, the ionisation parameter for the

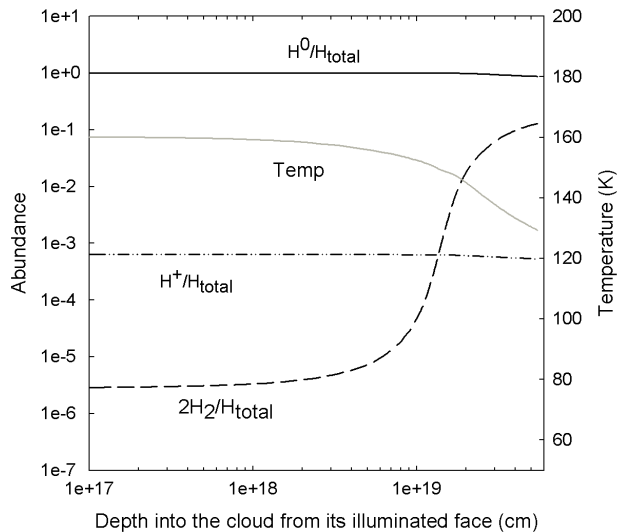


Figure 3. Temperature and H^0/H_{total} , H^+/H_{total} , $2H_2/H_{total}$ are plotted as a function of distance into GRB-DLA 120815A (Case 2). The temperature axis is shown in the right.

powerlaw continuum also differs for these two cases. Our best model for case 1 and case 2 predicts value of $A_V \approx 0.65$ and 0.54 , respectively. This value is consistent with $A_V = 0.9 \pm 0.3$ as measured by Friis et al. (2015). Our best models predict the cosmic ray ionisation rate for hydrogen $0.36 \times 10^{-16} \text{ s}^{-1}$, same for both the cases.

In the fourth and fifth columns of Table 5 we compare our predicted column densities with the observed data for case 1 and case 2, respectively. As can be seen that our predicted column densities match very well with the observed values within the observed error bars. Previously Friis et al. (2015) reported column densities for two different b parameters, 1 and 10 km s^{-1} . Their $J=2, 3$ column densities differ by more than a dex for $b = 1$ and 10 km s^{-1} . Our best models uses micro-turbulence $b = 1 \text{ km s}^{-1}$ and the predicted $J = 2, 3$ column densities lie between their values. We check a model with $b = 10 \text{ km s}^{-1}$, but the results for $J = 2, 3$ column densities do not differ much. Keeping in mind, the uncertainty of dust grain sizes at high-redshift, two additional models are also considered with half and double the size of ISM grains. However, none of those give the desired effect of reproducing the observed $J = 2, 3$ column densities. In Table 6 we present the change in predicted column densities (in dex) by varying important parameters by 0.3 dex around the value used in the best model. Since the result is similar for both the cases, we show results for Case 1 only. It is to be noted that like the previous GRB-DLA, among all the parameters, the effect of dust grains is the maximum. Temperature (solid grey), and abundances of H^0/H_{total} (solid-black), H^+/H_{total} (black-dotted), $2H_2/H_{total}$ (black-dashed) are plotted in Figs. 4 and 5 as a function of distance into the cloud for case 1 and case 2, respectively. It can be seen that the H_2 fraction starts to increase beyond 10^{19} cm from the illuminated

Table 4. Physical parameters of GRB-DLA 121024A using CLOUDY.

Physical parameters	best values	best values
	Case 1	Case 2
Power law: $\log(\chi)$	-3.3	-2.8
Black body: Temp (log K), $\log(\chi)$	4.9, -2.5	4.9, -2.5
Density $n(H) \text{ (cm}^{-3}\text{)}$	100	60
Cosmic ray ionisation rate (10^{-16} s^{-1})	0.4	0.4
[Fe/H]	-1.6	-1.6
[Mg/H]	-1.0	-1.0
[Ca/H]	-2.6	-2.6
[Zn/H]	-0.9	-0.9
[Ni/H]	-1.5	-1.5
[Mn/H]	-1.8	-1.8
[Cr/H]	-1.4	-1.4

Table 5. Comparison of observed and predicted column densities GRB-DLA 121024A (in log scale) using CLOUDY.

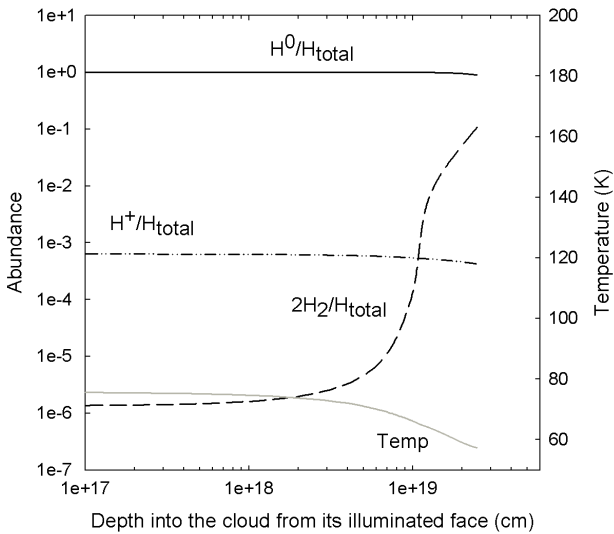
Species	observed	observed	predicted	predicted
	$b=10$ (cm^{-2})	$b=1$ (cm^{-2})	$b=1$ (cm^{-2}) Case1	$b=1$ (cm^{-2}) Case2
H I	-	21.6	21.77	21.69
H ₂	-	19.90	19.90	19.90
Mg I	-	<13.86	13.56	13.44
Ni II	-	14.47 ± 0.06	14.54	14.45
Zn II	-	13.47 ± 0.04	13.52	13.43
Ca II	-	12.40 ± 0.12	12.40	12.37
Fe II	-	15.58 ± 0.03	15.63	15.55
Mn II	-	13.47 ± 0.03	13.51	13.43
Cr II	-	13.97 ± 0.03	14.03	13.94
CO	-	-	10.93	11.26
HCl	-	-	12.28	12.18
H ₂ (0)	19.7	19.7	19.69	19.63
H ₂ (1)	19.2	19.3	19.47	19.55
H ₂ (2)	16.1	18.3	17.72	17.83
H ₂ (3)	16.0	18.2	17.21	17.83
H ₂ (total)	19.8	19.9	19.90	19.90

face of the cloud. For our best model of case 1, temperature varies between 73 K to 57 K with a mean of 65 K averaged over the linear thickness of the cloud, which matches well with the observed excitation temperature T_{10} at 60K. We also calculate the excitation temperature of the hyper-fine levels involved in 21 cm transition and found it to be $T_{21\text{cm}} = 1370 \text{ K}$, which is much higher than the kinetic temperature. Furthermore, our best model predicts the linear size of the GRB-DLA 121024A to be nearly 16 parsec for case 1.

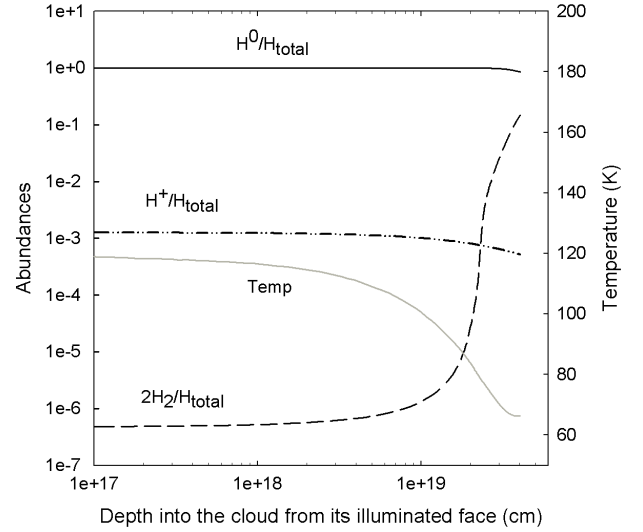
For the one-sided radiation field model, the predicted size of the DLA is found to be nearly 13 parsec. Also we find the gas temperature is 111 K at illuminated face of the cloud and it decreases to 66 K at the shielded face of the cloud with an average of 86 K over the linear size of the cloud. Furthermore we find that like the previous source, here $T_{21\text{cm}} \approx 1800 \text{ K}$, which is higher than the kinetic temperature. It is to be noted that here also both the gas temperature and the $T_{21\text{cm}}$ is higher for Case 2 than Case 1. For both the cases, the grain photoelectric heating is found to be the main source of heating, whereas the main sources of cooling

Table 6. Variation in column density of GRB-DLA 121024A (in dex) for variation in different input parameters (Case 1).

Species	$\Delta n(\text{H})$	Δ_{grain}	$\Delta \log(\chi)$ power law -0.3 dex
0.3 dex	0.3 dex	0.3 dex	
H I	0.02	-0.31	-0.15
Mg I	0.02	-0.37	-0.06
Ni II	0.01	-0.31	-0.15
Zn II	0.02	-0.30	-0.15
Ca II	0.04	-0.35	-0.01
Fe II	0.02	-0.33	-0.15
Mn II	0.03	-0.29	-0.15
Cr II	0.02	-0.30	-0.15
CO	0.16	0.71	0
HCl	0.01	0.08	0.15
H ₂ (0)	-0.03	-0.16	0.02
H ₂ (1)	0.04	0.18	-0.10
H ₂ (2)	0.06	0.17	-0.15
H ₂ (3)	0.26	0.03	-0.29

**Figure 4.** Temperature and $\text{H}^0/\text{H}_{\text{total}}$, $\text{H}^+/\text{H}_{\text{total}}$, $2\text{H}_2/\text{H}_{\text{total}}$ are plotted as a function of distance into GRB-DLA 121024A (case 1). The temperature axis is shown in the right. This plot shows half of the cloud. The other half is just the reflection of this portion.

points to C II line. Like the previous GRB-DLA, this GRB-DLA is also denser, smaller, and cooler than that reported by [Ledoux et al. \(2009\)](#) for GRB-DLAs with no H_2 .

**Figure 5.** Temperature and $\text{H}^0/\text{H}_{\text{total}}$, $\text{H}^+/\text{H}_{\text{total}}$, $2\text{H}_2/\text{H}_{\text{total}}$ are plotted as a function of distance into GRB-DLA 121024A (Case 2). The temperature axis is shown in the right.

4 SUMMARY AND CONCLUSIONS

GRB afterglows provide an unique opportunity to study the interstellar medium of star-forming galaxies at high-redshift. Observationally many GRB-DLA show H_2 , the main constituent of molecular clouds where star formation takes place. However, till date there is no detail study, incorporating quantum mechanical microphysics, on these systems to model H_2 lines. In this work for the first time we carry out such a study using spectral synthesis code CLOUDY, by modelling the observed column densities ([Friis et al. 2015](#)) of GRB-DLA 121024A and GRB-DLA 120815 ([Krühler et al. 2013](#)) self-consistently. We select these two specific H_2 -bearing GRB-DLAs, situated at redshifts 2.30 and 2.36 respectively, as they have substantially large H_2 molecular fraction. While the gas is exposed to UV radiation from everywhere it is exposed to GRB afterglow only from one side. Since the current CLOUDY set up does not allow to include both one-sided and two-sided radiation field simultaneously in a given model, we consider two cases separately. In Case 1, we assume that the gas cloud is irradiated from both sides, whereas in Case 2 we assume that the gas cloud is irradiated from one side. We present results for both the cases. The first number in the parenthesis represents Case 1 and the second number represent Case 2, respectively. We will follow this convention throughout.

- The total hydrogen density, consisting of ionised and atomic hydrogen together with all the hydrogen bearing molecules, are found to be (440, 230) and (100, 60) cm^{-3} for GRB-DLAs 120815 and 121024A, respectively. Earlier, [Ledoux et al. \(2009\)](#) estimated a particle density of 5-15 cm^{-3} for seven $z > 1.8$ GRB afterglows of their sample which did not show H_2 . Hence, our findings strongly suggest that the total hydrogen densities of H_2 -bearing GRB-DLAs are higher than that of without H_2 GRB-DLAs. This finding is also very much consistent with the recent observation of [Bolmer et al.](#)

(2019) who indicated that the GRB-DLA's gas pressure is higher and conversion of H I to H₂ occurs there.

- Earlier, [Ledoux et al. \(2009\)](#) estimated a linear cloud size of 520^{+240}_{-190} pc for GRB-DLAs lacking H₂. Here we find that linear sizes of H₂-bearing GRB-DLAs, 120815A and 121024A, are (9.8, 17.7) and (16, 13) pc, respectively. Taking together this also suggests that the linear sizes of H₂-bearing GRB-DLAs are smaller than that without H₂ GRB-DLAs. [Noterdaeme et al. \(2018\)](#) had also concluded that H₂-bearing QSO-DLAs have small physical extent.
- [Ledoux et al. \(2009\)](#) estimated that the kinetic temperatures of the metal-poor H₂ lacking GRB-DLAs are more than 1000 K. Our results suggest that the gas temperatures of H₂-bearing GRB-DLAs are lower than that of GRB-DLAs without H₂.
- The higher density, lower temperature and smaller physical extension as mentioned above suggests that the H₂-bearing GRB-DLAs trace the cold neutral phase of the ISM.
- Most of the heating to the environment of these systems is contributed by photoelectric heating.
- Most of the cooling of these systems is contributed by O I and C II lines.
- We find A_v values (0.32, 0.31) and (0.65, 0.54) for GRB-DLAs 120815 and 121024A, respectively. A_v > 0.1 for both the sight lines are consistent with the measurement of [Bolmer et al. \(2019\)](#).
- The cosmic ray ionization rate for hydrogen along the lines of sight for GRB-DLAs 120815 and 121024A are $(1.9 \times 10^{-16}, 1.9 \times 10^{-16})$ s⁻¹ and $(0.4 \times 10^{-16}, 0.4 \times 10^{-16})$ s⁻¹, respectively.
- The predicted column densities match very well with observed data except for the H₂ (*J*) = 2 level for GRB-DLA 120815A. In case of GRB-DLAs 121024A, Case 1 predicts H₂ (*J*) = 0, 1 levels better whereas Case 2 predicts H₂ (*J*) = 2, 3 levels better. Hence, only the temperature of these sources are constrained by the H₂ (*J*) = 0, 1 levels.
- Besides the observed species, the best model for GRB-DLA 120815A predicts OH and OH⁺ column densities to be more than 10¹³ cm⁻³. It will be interesting if this prediction gets verified by future observations.
- We find that the 21 cm spin temperature is higher than the gas kinetic temperature for both these sources, though observationally the 21 cm absorption line has not been found yet for none of them. It is to be noted that similar trend had also been observed for the QSO-DLA at redshift 1.78 along Q1333+ ([Chengalur & Kanekar 2000](#); [Cui et al. 2005](#)). In future, 21 cm absorption can be observed for GRB-DLAs using LOFAR or SKA.

In future, following this study, we will investigate more such H₂-bearing DLAs, some of which have recently been observed ([Bolmer et al. 2019](#)). It will be interesting to find whether our results also hold in general for all other H₂-bearing DLAs. That may help us to gain significant insights into the physical conditions of these important astrophysical systems and to understand why they possess molecular hydrogen, the main constituent of molecular clouds where star formation takes place. That will be an important contribution to the physics of star formation at high-red shift.

ACKNOWLEDGEMENTS

Gargi Shaw acknowledges WOS-A grant (SR/WOS-A/PM-9/2017) from the Department of Science and Technology, India and also like to thank the Department of Astronomy and Astrophysics, TIFR for its support. We would also like to thank the referee for his/her valuable comments and suggestions.

REFERENCES

- Abgrall, H., Roueff, E., & Drira, I., 2000, *A&AS*, 141, 297
 Abgrall, H., Le Bourlot, J., Pineau Des Forets, G., Roueff, E., Flower, D. R., & Heck, L., 1992, *A&A*, 253, 525
 Balashev, S. A. et al., 2017, *MNRAS*, 440, 225
 Balashev, S. A., Noterdaeme, P., 2018, *MNRAS*, 478, 7
 Bigiel, F., Leroy, A., Walter, F. et al., 2008, *AJ*, 136, 2846
 Bolmer, J., Ledoux, C., Wiseman, P., et al., 2019, *A & A*, 623, 43
 Black, J. H., & van Dishoeck, E. F., 1987, *ApJ*, 322, 412
 Burton, M. G. 1992, *Australian Journal of Physics*, 45, 463
 Chengalur, J. N., & Kanekar, N., 2000, *MNRAS*, 318, 303
 Cucchiara, A. et al., 2015, *ApJ*, 804, 51
 Cui, J., Bechtold, J., Ge, J., & Meyer, D. M., 2005, *ApJ*, 633, 649
 Dabrowski, I., 1984, *Canadian J. Phys.*, 62, 1639
 Whalen, D., Prochaska, J. X., Heger, A. et al., 2008, *ApJ*, 682, 1114
 D'Elia, V. et al., 2014, *A & A*, 564, 38
 Deguchi, S., & Watson, W. D., 1985, *ApJ*, 290, 578
 Draine, B. T., & Bertoldi, F., 1996, *ApJ*, 468, 269
 Ferland, G. J., Porter, R. L., van Hoof, P. A. M., et al., 2013, *RMxAA*, 49, 137
 Ferland, G. J., Chatzikos, M., Guzman, F., et al., 2017, *RMxAA*, Field, G. B., 1959, *ApJ*, 129, 536
 Friis, M. et al., 2015, *MNRAS*, 451, 157
 Fynbo, J. P. U., Prochaska, J. X., Sommer-Larsen, J., Dessauges-Zavadsky, M., MÅyler, P., 2008, *ApJ*, 683, 321
 Gay, C. D., et al., 2012, *ApJ*, 746, 68
 Gerlich, D., 1990, *J. Chem. Phys.*, 92, 2377
 Hartoog, O. E., et al., 2015, *A & A*, 580, 139
 Haardt F., Madau P., 2012, *ApJ*, 746, 125
 Heintz, K. E., Ledoux, C., Fynbo, J. P. U., et al., 2019, *A & A*, 621, 20
 Indriolo N., Geballe T. R., Oka T., McCall B. J., 2007, *ApJ*, 671, 1736
 Krstic, P. S., 2002, *Phys. Rev. A*, 66, 042717
 Krühler, T. et al., 2015, *A & A*, 581, 125
 Krühler, T. et al., 2013, *A & A*, 557, 18
 Komasa, J. et al., 2011, *JCTC*, 7(10), 3105
 Launay, J. R., Le Dourneuf, M., & Zeippen, C. J., 1991, *A & A*, 252, 842
 Li, L., Wang, Y., Wu, X., Huang, Y., Zhang, B., Ryde, F., Yu, H., 2018, *ApJS*, 234, 26
 Le Bourlot, J., Pineau des Forets, G., Roueff, E., Dalgarno, A., & Gredel, R., 1995, *ApJ*, 449, 178
 Le Bourlot, J. Z., 1991, *A & A*, 242, 235
 Ledoux, C., Vreeswijk, P. M., Smette, A., Fox, A. J., Petitjean, P., Ellison, S. L., Fynbo, J., P. U., Savaglio, S. 2009, *A & A*, 506, 661
 Ledoux, C., Petitjean, P., & Srianand, R., 2003, *MNRAS*, 346, 209
 Mathis J. S., Rumpl W., Nordsieck K. H., 1977, *ApJ*, 217, 425
 Marasco, A., Fraternali, F., van der Hulst, J. M., Oosterloo, T., 2017, *A & A*, 607, 106
 Porter, R. L., Ferland, G. J., Storey, P. J., & Detisch, M. J., 2012, *MNRAS*, 425, L28
 Noterdaeme, P., et al., 2014, *A & A*, 566, 24
 Noterdaeme, P., et al., 2015a, *A & A*, 577, 24

- Noterdaeme, P., Petitjean, P., Srianand, R., 2015b, *A & A*, 578, 5
- Noterdaeme, P., Ledoux, C., Petitjean, P., Le Petit, F., Srianand, R., & Smette, A., 2007, *A & A*, 474, 393
- Noterdaeme, P. et al., 2018, *A & A*, 612, 58
- Prochaska, J. X., & Wolfe, G., 2002, *ApJ*, 566, 68
- Prochaska, Jason X. et al., 2001, *ApJS*, 137, 21
- Prochaska, Jason X., Chen, Hsiao-Wen, Dessauges-Zavadsky, Mirosława, Bloom, Joshua S., 2007, *ApJ*, 666, 267
- Ranjan, A., et al., 2018, *A & A*, 618, 184
- Ranjan, A., et al., 2020, *A & A*, 633, 125
- Rawlins K., Srianand R., Shaw, G., 2018, *MNRAS*, 481, 2083
- G. B. Rybicki and A. P. Lightman, *Radiative processes in astrophysics*. New York, Wiley-Interscience, 1979, 393p
- Jorgenson, R. A., Wolfe, A. M., Prochaska, J. X., Carswell, R. F., 2009, *ApJ*, 704, 1
- Savage, B. D., Bohlin, R. C., Drake, J. F., & Budich, W., 1977, *ApJ*, 216, 291
- Schady, P., 2017, *RSOS*, 470304S
- Shaw, G., Ferland, G. J., Srianand, R., et al., 2008a, *ApJ*, 675, 405
- Shaw, G., Ferland, G. J., Abel, N. P., et al., 2005, *ApJ*, 624, 794
- Shaw, G., Ferland, G. J., Srianand, R., Abel, N. P., 2006, *ApJ*, 639, 941
- Shaw G., Rawlins K., Srianand R., 2016, *MNRAS*, 459, 3234
- Shaw, G., Ferland, G. J., Abel, N. P., et al., 2008b, *ApJ*, 624, 794
- Shaw, G., Ferland, G. J., Hubeny, I., 2017, *ApJ*, 843, 149
- Shaw, G., Bhattacharyya, S., 2019, *MNRAS*, 486, 195
- R. Srianand & P. Petitjean., 2000, *A&A*, 357, 414
- Sheffer, Y., Prochaska, J. X., Draine, B. T., et al., 2009, *ApJ*, 701, 63
- Srianand R., Shaw G., Ferland G., Petitjean P., Ledoux C., 2005a, *ArXiv Astrophysics e-prints*,
- Srianand R., Petitjean P., Ledoux C., Ferland G., Shaw G., 2005b, *MNRAS*, 362, 549
- Sternberg, A. 1988, *ApJ*, 332, 400
- Sternberg, Amiel; Le Petit, Franck; Roueff, Evelyne; Le Bourlot, Jacques, 2014, *ApJ*, 790, 10
- Sun, Y., & Dalgarno, A., 1994, *ApJ*, 427, 1053
- Takahashi, J., & Uehara, H., 2001, *ApJ*, 561, 843
- Tielens, A.G.G.M. 2005, *The physics and Chemistry of interstellar medium*, Cambridge university press, UK
- Tineé, S., Lepp, S., Gredel, R., Dalgarno, A., 1997, *ApJ*, 481, 282
- Tumlinson, J., et al., 2007, *ApJ*, 668, 673
- Toy, Vicki L., Cucchiara, Antonino., Veilleux, Sylvain., et al., 2016, *ApJ*, 832, 175
- Urbaniak, J.J., & Wolfe, A. M., 1981, *ApJ*, 244, 406
- Ubachs, W., et al., 2019, *A & A*, 622, 127
- van Hoof, P. A. M. 1997, PhD thesis, Rijksuniversiteit Groningen 905
- van Hoof, P. A. M., Weingartner, J. C., Martin, P. G., Volk, K., Ferland, G. J., 2004, *MNRAS*, 350, 1330
- Verela et al., 2016, *a&a*, 589, 37
- Welty, Daniel E.; Lauroesch, James T.; Wong, Tony; York, Donald G., 2016, *ApJ*, 821, 118
- Whalen, D.; Prochaska, Jason X.; Heger, A. & Tumlinson, J., 2008, *ApJ*, 682, 1114
- Wolfe A. M., Gwiser E., Prochaska J. X., 2005, *ARAA*, 43, 861
- Winkel, B., et al., 2017, *A & A*, 600, 2
- Woodsley, S. E., 1993, *ApJ*, 405, 273
- Zafar, T., et al., 2018, *MNRAS*, 480, 108

This paper has been typeset from a $\text{\TeX}/\text{\LaTeX}$ file prepared by the author.